



Experimental investigation of ablation and pyrolysis processes of carbon-phenolic ablators in atmospheric entry plasmas



Bernd Helber^{a,b,*}, Alessandro Turchi^a, James B. Scoggins^a, Annick Hubin^b, Thierry E. Magin^a

^a von Karman Institute for Fluid Dynamics, Chaussée de Waterloo 72, B-1640 Rhode-Saint-Genèse, Belgium

^b Vrije Universiteit Brussel, Pleinlaan 2, B-1050 Brussel, Belgium

ARTICLE INFO

Article history:

Received 22 September 2015

Received in revised form 10 December 2015

Accepted 20 April 2016

Keywords:

Charring ablator

Pyrolysis blowing

Surface ablation

Emission spectroscopy

Atmospheric entry

ABSTRACT

We study the ablation and transient pyrolysis outgassing of the carbon-phenolic ablators AQ61 and Asterm in air and nitrogen plasmas. We investigate their resistance to high heating conditions, and characterize gas-surface interaction phenomena, including the interaction of the pyrolysis gases with the hot plasma flow. The experiments were carried out in the Plasmatron facility of the von Karman Institute for Fluid Dynamics. The aero-thermodynamic environment of atmospheric entry in the boundary layer of a test object was selected with surface temperatures between 1900 K and 2800 K, and test chamber pressures of 15 hPa, 100 hPa, and 200 hPa.

Those conditions led to recession rates between 39 $\mu\text{m/s}$ and 83 $\mu\text{m/s}$ in air plasmas. Micrographs revealed oxidation of the char layer and carbon fibers. Carbon deposition in the form of soot was observed on samples tested in nitrogen, contrary to air ablation where charred resin was not found at the surface.

We propose an approach to estimate the temporally resolved pyrolysis outgassing rate, based on the emission signature of pyrolysis products and the volume change of the sample. The temporal recession rate was obtained from high-speed camera imaging. This enabled evaluation of the surface recession as a function of the pyrolysis outgassing rate, which was then compared to numerical estimates predicted by thermochemical equilibrium tables.

The thermochemical equilibrium model generally underpredicted experimental recession rates, particularly at low pressure (15 hPa). Stronger mechanical failure of the material was ruled out as experiments at the same test conditions in nitrogen plasmas did not show any significant recession. Micrographs did not indicate internal oxidation of the material, neither was spallation observed during the low pressure experiments.

© 2016 Elsevier Ltd. All rights reserved.

1. Introduction

On 6 August 2012, NASA's Mars Science Laboratory (MSL) mission successfully landed a rover on the Martian surface including an automated sample collection system for chemistry and mineralogy analysis. The next steps will be to identify, develop, and qualify required technologies for returning Martian and other asteroid samples safely to Earth.

Such sample return missions at very high re-entry speeds will use ablative materials for the Thermal Protection System (TPS), shielding the spacecraft from the severe heating during the atmospheric entry. The ablative Thermal Protection Material (TPM) is generally composed of a rigid precursor and a filling matrix, to

serve as a pyrolyzing, ablating, and insulating material at low weight with reasonable mechanical properties. During atmospheric entry, part of the heat flux is transferred inside the heat shield, and the virgin material is transformed following pyrolysis and ablation. Pyrolysis progressively carbonizes the phenolic resin into a low density, porous char, losing around 50% of its mass producing pyrolysis gases by vaporization. The pyrolysis gases are convected out of the material and exhaust into the boundary layer, providing a further barrier for the heat exchange by blowing and undergo additional chemical reactions. Ablation of the char layer, composed of the carbonized resin and the remaining carbon fibers, is then promoted by heterogeneous chemical reactions, phase change and mechanical erosion, altogether leading to recession of the material [1–3].

A new class of lightweight carbon-phenolic composites is being developed since the last decade, specifically designed for the high heating rates of planetary missions. A current example is made of a

* Corresponding author at: von Karman Institute for Fluid Dynamics, Chaussée de Waterloo 72, B-1640 Rhode-Saint-Genèse, Belgium. Tel.: +32 (0)2 359 96 27.

E-mail address: helber@vki.ac.be (B. Helber).

porous carbon fiber substrate impregnated with phenolic resin such as PICA (phenolic-impregnated carbon ablator) developed by NASA [4,5], and European ablators Asterm and AQ61, developed by Airbus DS [6]. Most recent examples for the successful performance of PICA are the Stardust [7], and MSL [8,9] missions. A similar ablator, PICA-X, is used for the Dragon spacecraft, designed by SpaceX for crew and cargo service of the ISS.

Selection and thickness definition of the TPM are the two key performance parameters in TPS design, and rely on predictions of the heat flux to the bondline of the spacecraft. But despite the advancements made since the Apollo missions to the moon, heat flux prediction remains an imperfect science and engineers resort to safety factors to determine the TPS thickness. This goes at the expense of embarked payload, hampering sample return missions [10]. Combined theoretical, numerical, and experimental research is required to improve our understanding of the complex gas/surface interaction and ablator material response in atmospheric entry flows. Ground testing in plasma wind-tunnels is currently the only affordable possibility for both material qualification and validation of material response codes. The goal of this work is to contribute to the ongoing efforts of improving the heat shield reliability, reducing design uncertainties and developing new thermochemical ablation models with new experimental data on porous, low-density ablators.

Most ground-based investigations of TPM have been carried out in arc-jet facilities [5,11–16], which offer high-enthalpy, supersonic plasma flows to reproduce stagnation pressure and peak heating on the material surface. This strategy allows qualification of a specific material in a confined test environment, and the design of material response models that match ground test data [17]. The averaged experimental data, usually recession, mass loss, and temperatures, are used to extract thermophysical properties of the heat shield material [14].

The total mass loss of charring ablators is composed of simultaneous char layer ablation and pyrolysis of the internal resin binder (Fig. 1). But transient phenomena, such as the rapidly changing blowing rates caused by strong internal pyrolysis, are usually not captured. Especially during start of the experiment, the strong temperature rise causes almost instant vaporization of the phenolic resin near the surface. For example, the time for PICA to reach steady-state ablation in arc-jet tests is on the order of 10 s [16]. During steady-state ablation, the speed at which the surface recesses equals the speed of the pyrolysis propagation towards the virgin material ($\dot{s}_c = \dot{s}_v$). Recent material response simulations of porous ablators focused on the transient behavior of the pyrolysis gas flow. Those studies demonstrated the strong influence of the sample geometry on the strength and direction of pyrolysis outgassing [18] as well as the importance to accurately model the pyrolysis gas flow for a correct temperature prediction [19]. In addition, state-of-the-art numerical models treat the pyrolysis

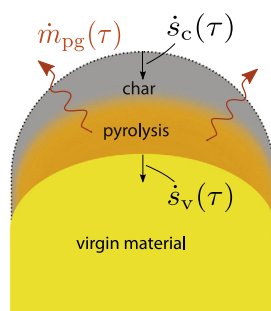


Fig. 1. Simplified schematic of mass losses in pyrolyzing ablator: Transient pyrolysis gas mass loss (\dot{m}_{pg}) inside the material leading to consumption of virgin material (\dot{s}_v), and char layer removal by recession (\dot{s}_c).

gas mixture as an average of decomposition products [20,21]. New high fidelity material response models are proposed to take into account the porous micro-structure of the new class of materials [22,23] as well as a non-constant elemental composition for the pyrolysis gas mixture [24,25].

The focus of our study will be the identification of the transient pyrolysis gas blowing rates for evaluation of the material recession in different air and nitrogen plasma environments. The subsonic 1.2 MW inductively coupled plasma (ICP) torch of the Plasmatron facility at the von Karman Institute (VKI) is able to reproduce the aero-thermodynamic environment of atmospheric entry in the boundary layer of a test object for a wide range of pressures and heat fluxes [26,27]. In a previous article we studied a porous, non-pyrolyzing carbon-bonded carbon preform [28], similar to the precursor of carbon-phenolic ablators such as Asterm. With this work, we extend our analysis towards phenolic-impregnated carbon ablators that may serve as TPM for future missions.

In particular, this work provides information on the following aspects:

1. Visual inspection including microscale analysis to identify ablation at the fiber scale (Section 3.1).
2. Thermal response of the material and ablation rates in air (Sections 3.2 and 3.3).
3. Tracing of pyrolysis products in the boundary layer (Section 3.4):
4. Suggestion of an experimental approach to track the transient pyrolysis gas blowing rate, enabling comparison of ablation rates with equilibrium thermochemistry (B' -tables) (Section 4).

2. Ablative materials and experimental methods

The experimental and numerical tools for this work are reviewed in this section. It includes presentation of the Asterm and AQ61 material samples, the Plasmatron facility together with experimental and numerical procedures to characterize the plasma flow field, as well as the experimental setup with description of the emission spectroscopy arrangement.

2.1. Ablative test samples

We tested two different carbon composites (Asterm and AQ61) made of short carbon fibers impregnated with phenolic resin as described below. Their geometry was a 25 mm radius hemisphere with a 25 mm (Asterm) or 20 mm (AQ61) long cylinder. In the subsonic plasma flow of the VKI Plasmatron, hemispherical ablative samples responded with a stable axial recession of the hemisphere, with low sidewall ablation [29]. This allows for constant boundary conditions throughout the whole experiment.

Astern is a low-density ablator, similar to NASA's PICA [4], developed by Airbus DS for future high-speed (re-) entry missions. It is manufactured by impregnating a rigid graphite felt preform with phenolic resin, followed by a polymerization process and final machining [6]. This approach significantly reduces the manufacturing effort and allows for large scale production over a large range of final material densities, from 240 kg/m³ to 550 kg/m³. The expanded structure of impregnated resin gives the material a low density and high porosity. We already presented other Plasmatron experiments of a similar non-pyrolyzing carbon fiber preform in another reference [28]. This carbon-bonded carbon fiber (CBCF) preform is made of short cut carbon fibers, interconnected in a fully carbonized matrix [30].

AQ61 is a generic ablative material previously developed by Airbus DS, representing a low density carbon-phenolic material. In contrast to Astern, AQ61 is not made up of one single piece of carbon

fiber preform but is manufactured by impregnating large pieces of carbon felts compressed to the right density during the impregnation process [6]. The cured AQ61 structure is more rigid than that of Asterm, has a higher density, and presents a lower resin content.

2.2. Plasmatron facility and flow characterization

The VKI Plasmatron facility has been used for the reproduction of the aero-thermodynamic environment of re-entry plasma flows, creating a high-enthalpy, highly dissociated subsonic gas flow. Previous ablation experiments on lightweight carbon-composites were carried out on the MonA ablator [31] and a Carbon-Bonded Carbon Fiber (CBCF) preform [28].

The Plasmatron is equipped with a 160 mm diameter Inductively Coupled Plasma (ICP) torch powered by a high frequency, high power, high voltage (400 kHz, 1.2 MW, 2 kV) generator (MOS technology). The gas is heated by induction through a coil, creating a high purity plasma flow. Three probe holders are installed in the Plasmatron facility next to each other, which can be exchanged independently by a pneumatic mechanism. One holds the ablative test sample, whilst the other two are used for heat flux and Pitot pressure measurements in the same experimental run as the ablation test. The cold wall (~ 350 K) stagnation point heat flux \dot{q}_{cw} was measured with a water-cooled calorimeter with a sensing element of 14 mm in diameter made of copper.

A water-cooled Pitot probe, connected to a Validyne variable reluctance pressure transducer, was used to determine the dynamic pressure of the plasma flow.

The subsonic Plasmatron flow-field was numerically simulated using a Navier–Stokes equation solver coupled with Maxwell equations for the electro-magnetic field created by the coil (VKI ICP code [32–34]). This provides hydrodynamic parameters (streamwise velocity v , boundary layer velocity gradient β , boundary layer thickness δ) as an initial characterization of the boundary layer around the test sample under Local Thermodynamic Equilibrium (LTE) and axisymmetric flow assumptions. The hydrodynamic boundary layer edge parameters, as well as the experimentally determined heat flux and Pitot pressure serve as input conditions for the VKI boundary layer code [35]. It solves the chemically-reacting stagnation line boundary layer over a catalytic surface under chemical non-equilibrium conditions, assuming a fixed wall

catalycity for copper (γ_{cw}) and a cold wall temperature (T_{cw}) for the heat flux probe. A more detailed description of this procedure applied to ablation tests can be found in another reference [28].

Two test gases have been used, air and nitrogen, the latter to restrict the number of chemical reactions at the wall. The duration of each test was chosen to maintain a similar heat load on the samples for all test cases. The mass flow was kept at $\dot{m} = 16$ g/s. For the results presented throughout this paper, the time indication $\tau = 0$ s corresponds to the injection of the test sample into the plasma flow. Plasmatron test conditions providing test gas, static and dynamic pressure, cold wall heat flux, boundary layer edge rebuilding, and ablation results are listed in Table 1.

The sample was attached to a sample holder located 445 mm downstream of the plasma jet exit in an actively cooled sample-conditioning system to prevent preheating and early pyrolysis. After reaching the favored test condition (test chamber static pressure and heat flux), the sample was inserted using a pneumatic mechanism.

2.3. Experimental methods for ablation characterization

A schematic of the experimental setup for freestream and in situ ablation measurements can be found in Fig. 2, and is reviewed below. We used a two-color Raytek Marathon MR1S-C pyrometer, employing a wide (0.75–1.1 μm) and narrow (0.95–1.1 μm) spectral band for the temperature determination at a 1 Hz acquisition rate (1300–3300 K). Using two narrow wavelength bands (two “colors”) and under the assumption of an emissivity being independent of the wavelength in the range 0.75–1.1 μm , temperature of the surface can be estimated without knowing the emissivity. The pyrometer was pointed and focused in the stagnation area of the sample through a 1 cm thick quartz window, at an angle of $\sim 35^\circ$ with respect to the stagnation line. The instrument was calibrated up to 3300 K at the National Physical Laboratory (London, UK) using a high temperature graphite blackbody, including a spot-size and uncertainty analysis, which resulted in $\delta T_w = \pm 15$ K in the observed temperature range. The highest uncertainty was attributed to the positioning of the pyrometer with respect to the quartz window, introducing measurement inaccuracies.

The bright surface was observed with a High-Speed Camera (HSC) for determination of the recession rates. The short exposure times (2 μs) of the Vision Research Phantom 7.1 CMOS HSC

Table 1
Plasmatron test conditions and main results: test case reference for materials AQ61 (AQ) and Asterm (AS), followed by test gas, static pressure p_s , dynamic pressure p_d , Plasmatron electrical power, mean cold wall heat flux \dot{q}_{cw} , flow enthalpy h_e , density ρ_e , temperature T_e , velocity v_e , exposure time τ and surface temperature T_w , recession rate \dot{s} , and total mass loss Δm .

Test ID	Gas	Probe measurements and boundary layer edge characteristics								Ablation experiments			
		Measurements				Simulation				τ (s)	T_w (K)	\dot{s} ($\mu\text{m/s}$)	Δm (g)
		p_s (hPa)	p_d (Pa)	P (kW)	\dot{q}_{cw} (kW/m ²)	h_e (MJ/kg)	ρ_e (g/m ³)	T_e (K)	v_e (m/s)				
AQ-A1a	air	15	135	161	1023	21.7	0.62	5474	228.7	90.4	2115	47	5.8
AQ-A1b	air	15	400	400	2994	52.0	0.27	9051	699.9	30.0	2765	47	4.0
AQ-A2	air	100	17.0	181	1038	21.6	3.86	5950	33.6	90.4	2080	46	4.9
AQ-A3a	air	200	6.20	158	1026	20.9	7.67	6090	13.9	90.3	1860	39	3.6
AQ-A3b	air	200	57.0	356	3058	42.0	4.32	8075	59.7	30.0	2790	83	3.8
AQ-N1a	N ₂	15	131	177	997	22.2	0.63	5586	223.1	90.5	1975	0.5	2.4
AQ-N1b	N ₂	15	263	354	3034	59.7	0.25	9217	586.0	30.4	2520	2.1	2.3
AQ-N2	N ₂	100	13.4	213	1017	23.2	3.83	6136	29.5	90.0	2005	0.6	1.8
AS-A1a	air	15	143	155	1010	21.1	0.63	5446	233.7	90.6	2080	58	8.0
AS-A1b	air	15	–	395	3000	53.1	0.26	9142	669.8	30.8	2740	62	5.8
AS-A2	air	100	15.5	184	977	20.5	3.98	5879	32.1	90.3	2050	54	6.7
AS-A3a	air	200	6.00	163	1016	20.7	7.72	6077	13.9	90.4	1845	35	5.5
AS-A3b	air	200	50.0	356	3200	44.7	3.93	8735	58.6	35.7	2735	71	6.0
AS-N1a	N ₂	15	131	175	995	22.2	0.63	5584	222.9	90.4	1995	0.2	4.5
AS-N1b	N ₂	15	200	337	3128	64.0	0.24	9504	526.6	30.4	2490	0	4.4
AS-N2	N ₂	100	13.1	215	1038	23.6	3.78	6159	29.6	90.0	2075	0	3.8

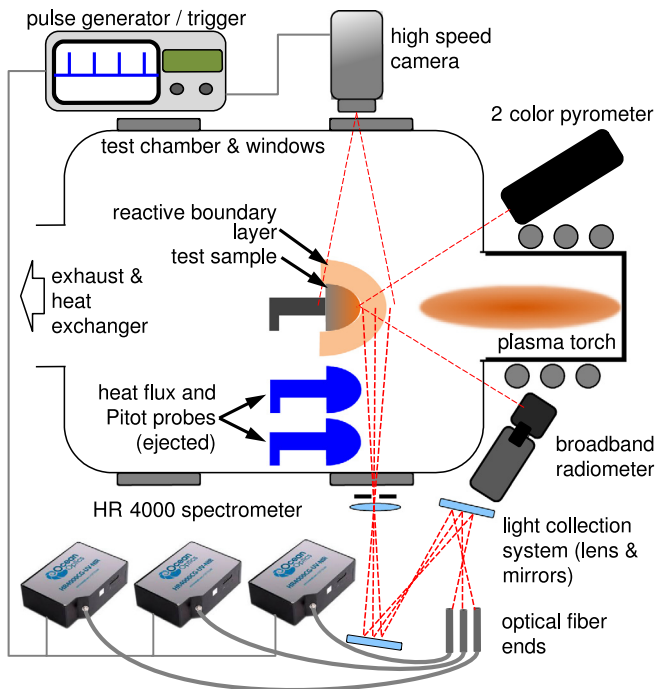


Fig. 2. Schematic of experimental setup showing the spectrometer optical paths perpendicular to the plasma flow ahead of the ablating sample (445 mm from plasma torch exit).

prevented sensor saturation and enabled an in situ recession analysis of the ablating test sample. It was moreover necessary to determine the location of the ablating surface in situ to enable evaluation of the emission spectroscopic measurements described shortly. Acquisition of the HSC was triggered using a Digital Delay Generator (DDG), synchronized with the Optical Emission Spectroscopy (OES) measurements, before injection of the test sample. This allowed for a precise determination of the total injection time.

Synchronized with the HSC were three Ocean Optics HR4000 spectrometers along the stagnation line for spatial information of the emission spectrum upstream of the test specimen. The optical diagnostic bench consisted of a light collection system, and one optical fiber for each of the three spectrometers. The light emitted by the plasma was collected through a variable aperture and focused by a plano-convex, uncoated fused silica lens (LA4745, 750 mm focal length) via two mirrors on the entry of the three optical fibers (Ocean Optics QP600-2-SR/BX, $600 \pm 10 \mu\text{m}$ core diameter). The optical path was aligned perpendicular to the flow and tangential to the test sample surface. The magnification of the optical system was set to $m = 3$ resulting in a distance between each probing volume of $\Delta d = 2 \text{ mm}$.

The AQ61 and Asterm samples were studied by SEM to investigate the in-depth char layer degradation and ablation of the carbon

fibers at microscale. A virgin sample of each material was first inspected, followed by inspection of the tested samples. The SEM system in use for this study was a Jeol JSM-6400 type of electron microscope. The standard working distance (WD) in imaging mode was set to 39 mm at an accelerating voltage of 20 kV. As the charred test samples are mostly composed of charred carbon, no further treatment, such as coating of the surface, is required. Tested samples were first inserted as a whole into the SEM's vacuum chamber to preserve the char layer for a first analysis. Then, the sample was cut along the stagnation line with a scalpel in order to study the sub-surface degradation.

3. Experimental results and discussion

Plasmatron test conditions (static and dynamic pressures p_s and p_d , electrical power P , and cold-wall heat flux \dot{q}_{cw}), boundary layer edge parameters (static enthalpy h_e , flow velocity v_e , gas density ρ_e , and temperature T_e), and ablation data (surface temperature T_w , recession rate \dot{s} , and total mass loss Δm) are summarized in Table 1. A Kern EW150-3M balance (1 mg precision) was used for pre- and post-test evaluations of total mass loss Δm . The surface temperature T_w is reported as the mean over the whole test time, and the recession rate \dot{s} is the slope obtained from the HSC during steady conditions.

3.1. Post-test visual inspection

The post-test photographs of Fig. 3 show a clear difference of two AQ61 test samples after ablation in air or nitrogen. Air ablation led to alteration of the outer char layer due to carbonization of the resin and ablation of the carbon fibers, especially visible on photographs of the sample backside. The central (darker) part was not fully carbonized with some content of phenolic resin left. The surfaces of the samples exposed to nitrogen plasma appeared gray to black and covered with soot. This was confirmed by post-test Scanning-Electron-Microscopy (SEM) as will be seen below.

The appearance of Asterm samples changed from the virgin yellow to black after the ablation test due to charring (Fig. 4(a)). Cut Asterm samples revealed that most of the virgin material had been pyrolyzed (Fig. 4(c)), except a small portion at the backside, probably caused by the water-cooled holding stem the sample was mounted on. However, the color of partially charred Asterm does not give quantitative information about its charring level. For example, the coloring of charred PICA becomes blackish once approximately 50% of the material is charred [17]. A thin layer of soot covered the surface of Asterm samples tested in nitrogen (Fig. 4(d)).

Closer observation of cut Asterm samples (Fig. 4(c)) reveals slight differences in the char layer color, with a light-gray at a certain material depth (approximately 5 mm to 10 mm from the surface). This might be a result of different char layer compositions,

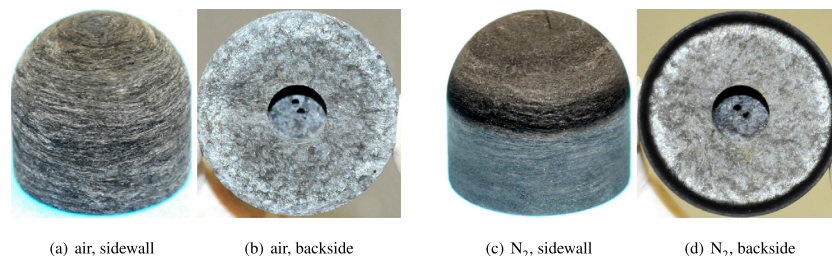


Fig. 3. Post-air ablation photographs of AQ61, exposed to a cold wall heat flux of $\dot{q}_{cw} = 3 \text{ MW/m}^2$ and a chamber static pressure of $p_s = 15 \text{ hPa}$ in an air ($T_w = 2765 \text{ K}$) and nitrogen ($T_w = 2520 \text{ K}$) atmosphere for 30 s.

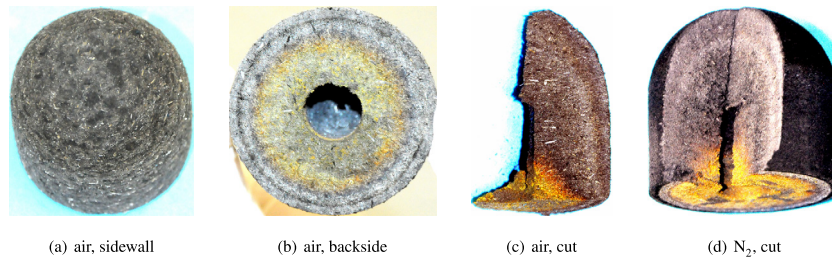


Fig. 4. Post-air ablation photographs of Asterm show carbonized surface with change of color from yellow to black ($T_w = 2740$ K), cut samples (c) reveal an almost completely charred test sample (3 MW/m^2 , 15 hPa); the nitrogen tested sample (d) illustrates soot formation at the surface ($T_w = 2490$ K). (For interpretation of the references to colour in this figure caption, the reader is referred to the web version of this article.)

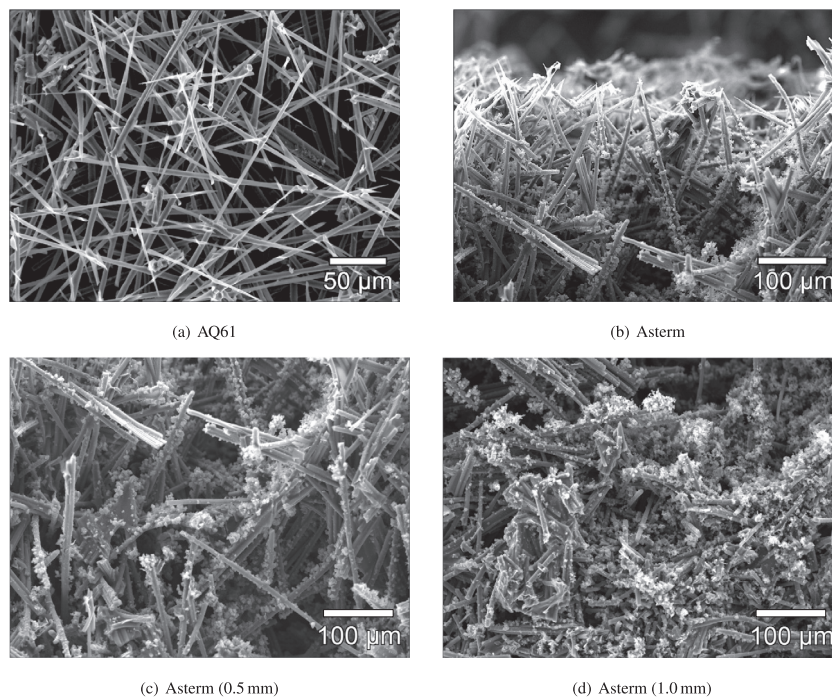


Fig. 5. Surface micrographs of AQ61 (a) after ablation in air depicts icicle shaped fibers with high porosity, no charred resin was identified at surface (AQ-A1a, 200 hPa , 1 MW/m^2); Section-cut micrograph of Asterm (b) depicts similar icicle shaped fibers due to oxidation with high porosity of the charred material. Charred resin was identified close to the surface and increased with material depth. The micrographs taken at depths of 0.5 mm (c) and 1 mm (d) highlight the high amount of charred resin but no oxidation of resin and fibers (AS-A3a, 15 hPa , 1 MW/m^2).

for example due to different char yields, and/or additional coking of the pyrolysis gas during its travel through the material.

Air oxidation of the char layer led to removal of the carbonized resin, followed by ablation of the carbon fibers, resulting in a brighter color for the char layer. Oxidation from the fiber tips resulted in strong thinning of the carbon fibers for both materials, leading to icicle shaping of ablated fibers (micrographs Fig. 5).

Shape and roughness change of ablated carbon fibers due to heterogeneous reactions, in particular, the typical icicle shape observed during this work, is reported in literature for various conditions and materials [36–39]. Charred, partially ablated resin was visible $\sim 50 \mu\text{m}$ to $100 \mu\text{m}$ below the surface of AQ61. In this zone, all charred resin was oxidized, followed by ablation of the carbon fibers. Accordingly, charred resin was identified below the surface in the case of Asterm but not at the tip of the fibers (Fig. 5(b)). The amount of charred resin increased in-depth of the material (Fig. 5 (c) taken at 0.5 mm and Fig. 5(d) taken at 1 mm), but no quantitative analysis was performed. We further did not observe any internal oxidation of the charred resin, which, for example, would indicate an inflow of boundary layer gases. Lachaud et al. showed

that the internal pressure created by the pyrolysis gases leads to the blockage of boundary layer gases [19].

Micrographs of samples exposed to nitrogen revealed corrosion of the carbon fibers along the whole fiber length without significant recession. In addition to this, a web of thin “cross filaments” (nanometer scale) in-between carbon fibers was visible at the stagnation point of the tested samples (Fig. 6).

Due to the lack of oxygen, most of the carbonized resin remained as a connecting matrix in-between the carbon fibers. Micrographs proved that the sidewall of samples after nitrogen exposure was darkened by agglomerated carbon particles, forming soot at the surface (Fig. 7(b)). At the rear wall of the test specimen, the carbon fibers were augmented and thickened with charred resin in a small zone along the radius (Fig. 7(c)).

Both the carbon filaments and soot at the surface are assumed to be a result of carbon deposition from the pyrolyzed phenolic resin, that is not consumed by combustion in the gas-phase and condenses at the surface. Soot formation in flames is prominent in the combustion literature and an omnipresent byproduct in oxygen-poor environments. Many pathways exist for soot forma-

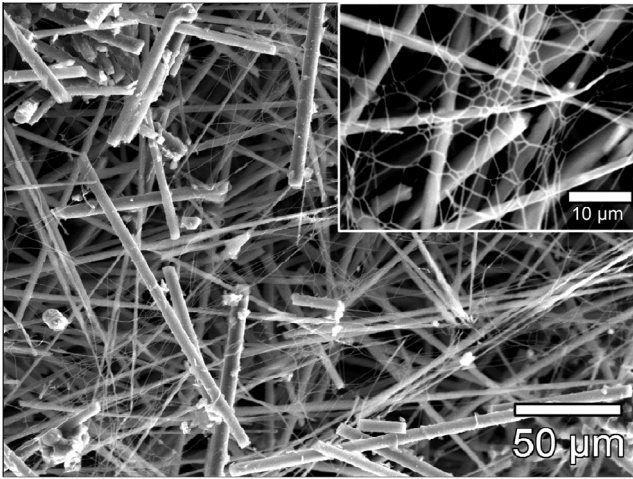


Fig. 6. Post-nitrogen micrograph of AQ61 (AQ-N1a) presents nano-scale “cross filaments” at the surface.

tion and Wang recently presented a summary of the formation of condensed-phase materials [40]. Important factors in soot formation are a high temperature environment as well as the presence of acetylene (C₂H₂). Evidence supporting the presence of acetylene may lie in the findings of C₂ in the gas-phase (Section 3.4). However, we found soot formation on a non-pyrolyzing carbon-bonded carbon fiber preform in a previous study [28]. The thin carbon filaments observed in the stagnation point may therefore be a result of condensation, for example of CN produced by nitridation, at the surface. Condensation of pure carbon molecules, such as C, C₂, C₃, is more likely at higher temperatures, when the surface reaches sublimation.

3.2. Surface and in-depth temperatures

Fig. 8 presents the surface- and internal-temperature responses of AQ61 samples in air and nitrogen plasmas at a cold wall heat flux of 1 MW/m² (a) and 3 MW/m² (b).

Surface temperatures quickly reached a quasi-steady state after injection into air and nitrogen plasma, resulting in maximum surface temperatures of 2765 K and 2530 K, respectively. Ablation of the char layer, and hence, a varying distribution of the surface carbon fibers, together with fluctuations of the plasma jet, caused fluctuations of the surface temperatures within 10 K to 20 K.

For the kind of materials under investigation, a steady burn-off rate is favored, keeping the high surface temperature at a constant value. Above roughly 3000 K, an increasing heat flux would rather cause higher surface recession than a surface temperature rise. At low heat flux (Fig. 8(a)), thermocouples were located 5 mm and 10 mm behind the initial stagnation point, but were changed to 10 mm and 20 mm for the higher heat flux test (b). Thermocouples of the same experiment recorded almost identical temperatures during the cool down phase once the heat wave had penetrated through the sample. Because the sample was shielded from the hot plasma during facility start-up by a water-cooled control system, initial temperatures did not exceed 360 K for any of the thermocouples prior to injection. Pyrolysis reactions do not take place at temperatures below 500 K and pre-charring of the test sample can thus be excluded.

3.3. In-situ recession analysis

The HSC captured recession of the ablating surface during the whole experiment for each test. The in situ recession for four conditions according to low/high pressure at low/high heating rates

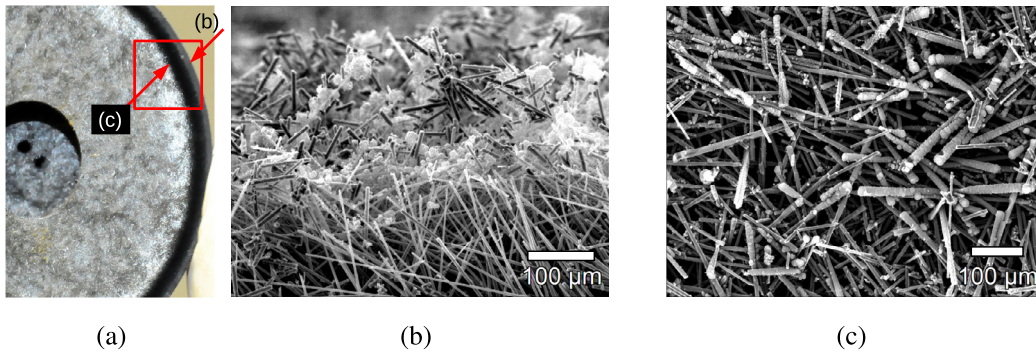


Fig. 7. Post-nitrogen-ablation photograph (a) and micrographs of AQ-N1b (N₂, 15 hPa, 3 MW/m²) highlighting soot at the sidewall (b) and agglomerated carbon fibers at the back side (c).

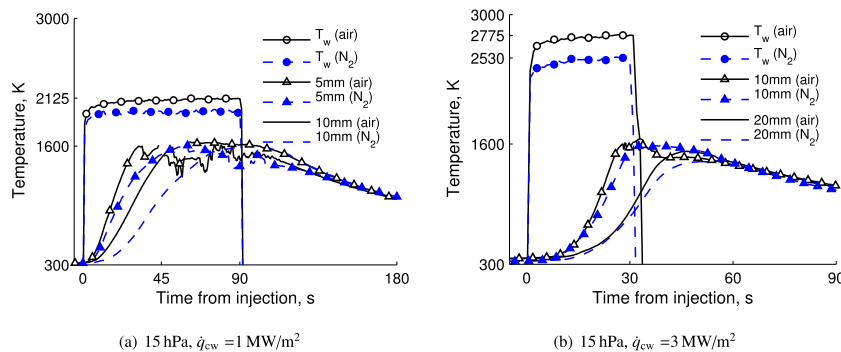


Fig. 8. Surface (T_w) and internal temperatures (5 mm and 10 mm at 1 MW/m² (a) and 10 mm and 20 mm at 3 MW/m² (b)) during AQ61 ablation are higher in air plasma (full lines) than in nitrogen (dashed lines) (AQ-A1a/b, AQ-N1a/b).

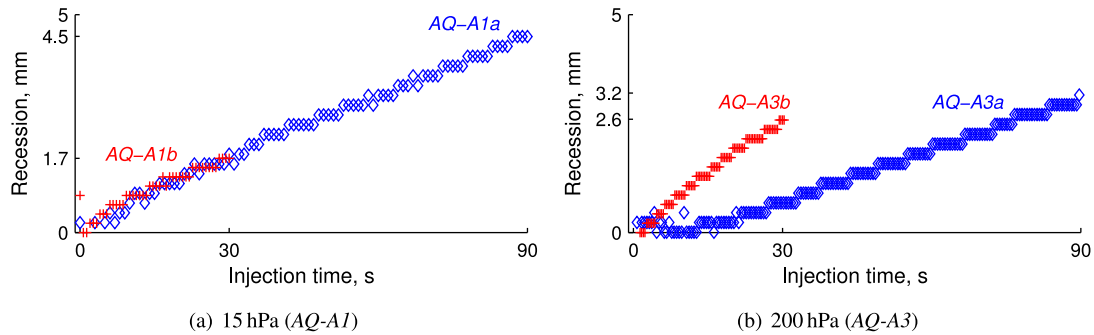


Fig. 9. AQ61 centerline recession in air at low (a) and high (b) pressure and heating conditions of 1 MW/m^2 and 3 MW/m^2 (a and b).

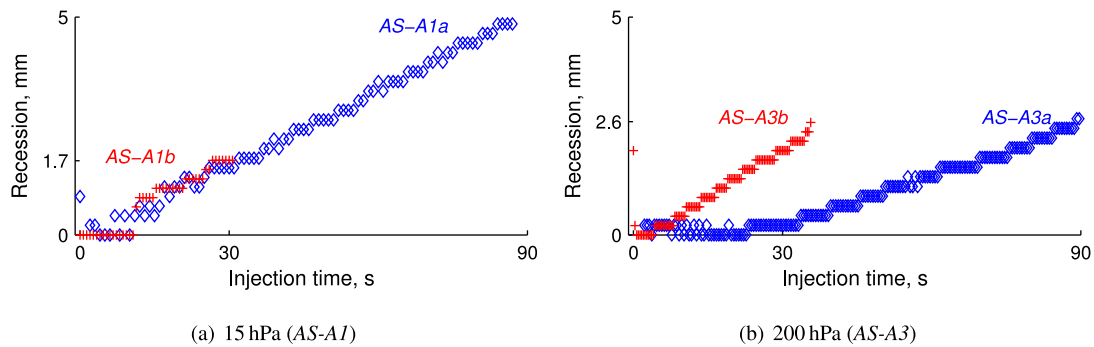


Fig. 10. Asterm centerline recession in air at low (a) and high (b) pressure and heating conditions of 1 MW/m^2 and 3 MW/m^2 (a and b).

are shown in Fig. 9(a) and (b) for AQ61, and in Fig. 10(a) and (b) for Asterm.

Both materials responded with very similar recession rates at low pressure, as well as at high heating rate in a high pressure environment (AS-A3b and AQ-A3b). At low heating but high pressure (A3a), AQ61 showed a slightly higher recession rate than Asterm. The data suggest similar AQ61 and Asterm recession rates at low pressure, independent of the heat flux (conditions A1, surface temperatures between 2080 and 2765 K), indicating a diffusion controlled ablation regime. Generally, a higher pressure would then lead to a higher carbon consumption and hence, a higher ablation rate. This was not seen in our case for low heating rates, where ablation rates at high pressure were lower than at low pressure (conditions A3a). However, recession rates for tests at high heat flux and high pressure (A3b) were considerably higher than at low pressure.

Figs. 9 and 10 also suggest that the surface began receding several seconds after injection, especially for the higher pressure condition AS-A3a. Here, the sample did not recede for the first 20 s. This might be either due to the thermal inertia and the required time to heat the sample, or to the strong pyrolysis outgassing at the beginning of the test, preventing recession. We presented in Fig. 8 the surface temperature response of AQ61 samples, which showed that the surface was almost instantly heated to high temperatures, only slightly rising during the test. Additionally, we will see below in Section 3.4 that pyrolysis blowing rates reached their maximum between 2 s and 3 s after sample injection.

Based on those two observations, (1) very fast heating of the surface and (2) strong pyrolysis gas blowing just after sample injection, we conclude that the delayed surface recession was caused by the ejection of pyrolysis gases into the boundary layer. Section 4 will present an approach to estimate the surface recession as a function of the pyrolysis gas blowing rate. The obtained results will be compared to a numerical ablation model based on equilibrium thermochemistry (B' -tables).

MacDonald et al. [41] also studied ablation of Asterm, at atmospheric pressure and surface temperatures of 2150 K and 2200 K. Their bulk Asterm material is reported with a density of 350 kg/m^3 , higher than ours. Their recession rate extracted from video imaging was $47 \text{ } \mu\text{m/s}$ for surface temperatures of approximately 2100 K at atmospheric pressure. This lies between our observations at similar surface temperatures for low (15 hPa: $58 \text{ } \mu\text{m/s}$) and high (200 hPa: $35 \text{ } \mu\text{m/s}$) pressures. Their initial sample shape was a cylinder, experiencing strong edge ablation over the 300 s test. This led to increasing surface temperatures during the first 60 s of the test, which became more uniform once the cylinder was ablated. This observation gives ground to the argument that the boundary layer thermochemistry was influenced during the experimental run by the shape change of the sample.

3.4. Temporal emission of ablation and pyrolysis products

A conventional photograph serves to illustrate the strong boundary layer emission in the visible wavelength range during ablation including pyrolysis gases (Fig. 11(a)). An emission spectrum taken in the boundary layer in front of the sample indicates dominant radiating molecules in the range 240–900 nm, most of them originated either from the pyrolysis gas ejection or the ablation process (Fig. 11(b)). Excited atomic oxygen and nitrogen from the plasma freestream were also identified. In general, the radiative spectrum was dominated by spontaneous emission of the electronically excited CN violet ($B^2\Sigma^+ \rightarrow X^2\Sigma^+$) system. At elevated surface temperatures, above 2600 K, atomic carbon was detected. We could further identify H_α and H_β lines of the Balmer series, and molecular systems including hydrogen as products from the phenol decomposition such as CH (A-X), NH (A-X) and OH (A-X), and carbon molecular systems like C_2 (Swan). Strong emission of the sodium (Na) doublet was observed around 589 nm for most of the experiments, which probably is a result of sample fabrication but also contamination due to machining. Main radiating tran-

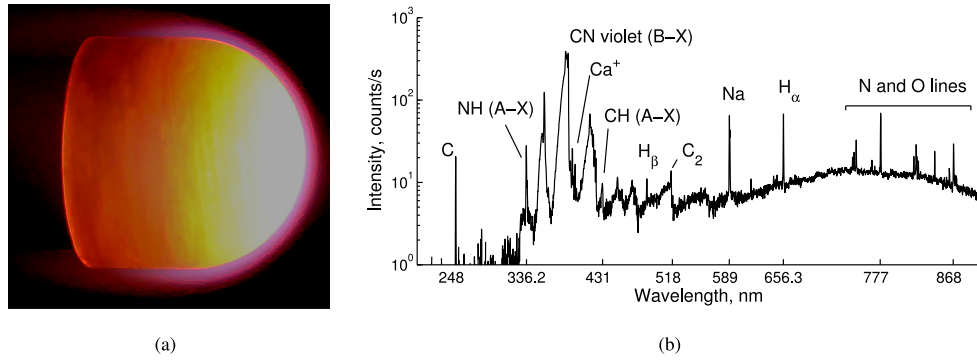


Fig. 11. (a) Strong boundary layer radiation in the visible wavelength range captured by photograph during AQ61 ablation; (b) Spectrally resolved emission during AQ61 ablation in air plasma (AQ-A1b) highlighting multiple species resulting from pyrolysis and ablation processes (3 MW/m², 15 hPa).

Table 2

Radiative transitions of electronically excited atomic and molecular species including C, H, Na, C₂, CH, CN, NH and OH.

Species	Transition	Wavelength, nm	Species	Transition	Wavelength, nm
C	1P ₁ → 1S ₀	247.8	C ₂	d ³ Π _g → a ³ Π _u (Swan)	516.2
H	3 → 2 (α)	656.3	CH	A ² Δ → X ² Π	431.4
H	4 → 2 (β)	486.2	CN	B ² Σ ⁺ → X ² Σ ⁺ (violet)	388.3
Na	2P _{1/2,3/2} → 2S _{1/2}	589.0	NH	A ³ Π → X ³ Σ	336.0
			OH	A ² Σ ⁺ → X ² Π	306.4

sitions are listed in Table 2. Wavelength indications for molecules refer to the vibrational 0–0 (bandhead) transition.

Line-of-sight averaged emission spectra can give valuable information about the decay of various emitting species and hence, the transient behavior of material decomposition throughout the experiment. To evaluate the temporal emission of atomic lines of species *i*, the emission signal $\epsilon(\lambda)$ was integrated with respect to the wavelength for each individual spectrum at time step $\Delta\tau$:

$$I_i^{(\Delta\tau)} = \int_{\lambda_1}^{\lambda_2} \epsilon(\lambda) d\lambda \propto \int_{\lambda_1}^{\lambda_2} n_u \frac{A_{ul}}{4\pi} \frac{hc}{\lambda_{ul}} d\lambda, \quad (1)$$

with the Einstein coefficient A_{ul} (atomic transition probability) and the number density of excited atoms n_u . Assuming LTE at temperature T , the population density of an upper state with degeneracy g_u is linked to the total species density N through a Boltzmann distribution,

$$n_u(T) = N(T) \frac{g_u \exp\left(-\frac{E_u}{k_B T}\right)}{Q_{int}}. \quad (2)$$

This shows that the (integrated) emission signal not only depends on temperature, but is also a function of the species concentration.

Hydrogen is a dominant product of phenol decomposition at high temperatures through dehydrogenation [42] and can be

probed via the strong H_α emission line (Fig. 11(b)). Normalized temporal emission profiles of H_α taken by the three spectrometers were almost identical, although taken 2 mm apart from each other in the boundary layer (Fig. 12(a)). Emission intensities increased away from the sample surface as is indicated by the maximum (calibrated) emission intensity of each curve in the legend. This might be a result of an increasing gas temperature in the boundary layer, leading to more excited states of hydrogen atoms according to Eq. (2). Dissociation of molecules containing hydrogen in the boundary layer may serve as another explanation. However, the normalized curves of Fig. 12(a) illustrate, that the temporal behavior of hydrogen emission is mostly driven by the transient pyrolysis gas injection, rather than being a function of the distance from the surface. Hydrogen emission showed the same temporal behavior as NH and C₂ (Fig. 12(b)). The Asterm composite has a higher phenolic resin content compared to AQ61, and therefore responds with higher pyrolysis outgassing at elevated temperatures. For this reason, the temporal emission profiles are only shown for Asterm.

Emission was clearly strongest at test start, probably due to the high injection of pyrolysis gases, and then decreased with progressing pyrolysis inside the material along with less outgassing. All emission profiles were similar for AQ61 and Asterm in both air and nitrogen plasmas, showing very similar temporal trends independent of the test gas.

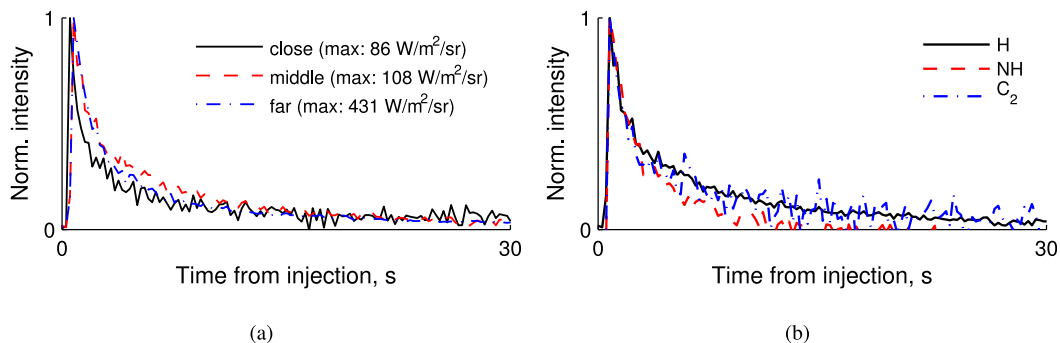


Fig. 12. (a) The normalized temporal emission profiles of H_α are identical for the three spectrometers (max. intensity indicated), hence, do not depend on distance from the surface; (b) H, NH, and C₂ temporal profiles recorded during Asterm ablation (middle spectrometer) in air plasma are identical, confirming the pyrolysis gas origin (AS-A1b).

The C₂ Swan system was also identified by emission spectroscopy during ablation testing of the carbon-phenolic ablator PICA [43], MonA [31], and AQ60 [44]. In the latter reference, C₂ emission is interpreted as a result from carbon particles that sublimate in the boundary layer. We have presented atomic carbon emission, most probably caused by sublimation, for a non-pyrolyzing CBCF preform material in another reference [28]. No traces of C₂ had been observed in that case. Based on those grounds, we relate the here observed C₂ emission to the hydrocarbon molecules ejected by the pyrolyzing material. From hydrocarbon chemistry it is known that C₂ is a dissociation product of C₂H₂, and C₂ spectra are prominent in high-temperature processes such as combustion and gas-phase pyrolysis. Two carbon atoms of acetylene are bonded together in a strong triple bond, breaking up at higher temperatures into C₂ and H [45]:



Those mechanisms support our argument that the C₂ Swan emission originated from the phenolic decomposition. Especially during the start of the ablation test, the virgin material at the surface is almost instantly heated above 2000 K, leading to vaporization and a fast consumption of the vaporized phenolic binder in the boundary layer.

Accordingly, the atomic carbon emission recorded at 248 nm suggests sublimation of the char layer. Reactions (3) and (4) also serve to explain the recorded hydrogen signal (H_α and H_β). Experimentally recorded hydrogen emission increased away from the surface, most probably due to the temperature increase leading to dissociation of the hydrocarbons.

Few similar studies of the emission signature during Asterm ablation are available in the literature. MacDonald et al. [41] studied ablation in the UV/VIS range of Asterm. They also observed CN violet emission close to the ablator surface and atomic oxygen emission decreased gradually from the freestream towards the ablator surface. From this, they concluded a boundary layer thickness of approximately 5 mm. In line with our study, the authors observed sodium and calcium in the boundary layer and also assigned this to material contamination.

Hermann et al. [46] studied the coupled effects of ablation and radiation in a magnetoplasma dynamic arcjet. They studied ablation of the non-pyrolyzing CBCF preform as well as pyrolyzing Asterm. Although the experiments were still preliminary, the authors report reduced VUV radiation caused by the carbon-phenolic material, suggesting absorption of incident radiation by the released pyrolysis gases. Conversely, Asterm ablation resulted in a higher emission signature in the UV/VIS spectral range, compared to a cold copper probe. Strong CN violet emission was observed in this case but the authors do not report on C₂ Swan emission, which might have been produced during the first test seconds in their case. Unfortunately, no temporal behavior of the emission in front of the pyrolyzing material is reported.

4. Ablation rate comparison with thermochemical equilibrium tables

This section first outlines the experimental approach for determination of in situ pyrolysis gas blowing rates. Secondly, we describe the numerical procedure for computation of the ablation rate based on different pyrolysis outgassing rates and gas compositions. The numerical approach is based on thermochemical ablation tables at equilibrium (B'-tables).

Table 3

AQ61 and Asterm mass loss due to pyrolysis outgassing only (m_{pg}) and its percentage contribution to total mass loss.

Test ID	T_w , K	p_s , hPa	m_{pg} , g	$\frac{m_{pg}}{\Delta m_{tot}}$, %
AQ-A1a	2115	15	1.12	23
AQ-A1b	2765	15	1.77	44
AQ-A2	n/a			
AQ-A3a	n/a			
AQ-A3b	2790	200	2.26	60
AQ-N1a	1975	15	2.37	100
AQ-N1b	2520	15	2.27	100
AQ-N2	2005	200	1.82	100
AS-A1a	2080	15	4.79	60
AS-A1b	2740	15	4.24	73
AS-A2	2050	100	4.32	65
AS-A3a	1845	200	4.04	74
AS-A3b	2735	200	4.83	81
AS-N1a	1995	15	4.53	100
AS-N1b	2490	200	4.44	100
AS-N2	2075	200	3.81	100

4.1. Experimental approach

Before comparing the experimental recession data with computed ablation curves, it is essential to know the temporal pyrolysis blowing rate during each experiment, which strongly impacts the surface thermochemistry and ablation rate. To do so, we determined the volume loss of ablated samples from HSC images. The pixel:mm conversion was determined using a mm-resolved chessboard, placed at the initial sample location. Assuming axisymmetric ablation, it was possible to determine the volume loss by integration of the extracted profile, and to study the shape change [29]. From the density of the charred material ρ_c , it was possible to estimate the total mass loss solely caused by degradation of the phenolic resin through pyrolysis m_{pg} by

$$m_{pg} = \Delta m_{tot} - V_{abl} \cdot \rho_c, \quad (5)$$

with the ablation volume loss V_{abl} from the HSC contour, and the total mass loss Δm_{tot} from post-test weighing of the sample (Table 1). We used the non-pyrolyzing carbon preform in another reference to examine the validity of this technique [29]. In that non-pyrolyzing case, mass loss estimated from HSC images ($V_{abl} \cdot \rho_c$) should be identical to the weighted one (Δm_{tot}) because only carbon fiber removal led to mass loss. Note that this only holds true if a density change, e.g., by volumetric ablation, does not occur, i.e., oxygen is not diffusing into the porous medium.

In addition, mass loss during ablation in nitrogen atmosphere was assigned to pyrolysis only, as recession of the surface proved sufficiently low (Table 1). Those values were used as indication for comparison with the pyrolysis blowing rates obtained during air ablation. The results of this analysis are presented in Table 3, separated for AQ61 and Asterm.

The mass loss m_{pg} represents an integration over the whole test time as it is computed from the total mass loss m_{tot} (Eq. (5)). To obtain temporally resolved pyrolysis gas blowing rates, we made use of the hydrogen time-profile provided by the spectrometer (Fig. 12(a)). From Eq. (1) we can assume that the intensity of hydrogen is directly related to the number of hydrocarbons ejected into the boundary layer, and therefore, to the strength of pyrolysis outgassing. We support this assumption with the identical temporal H_α-profiles at various distances from the surface (Fig. 12(a)), and the identical temporal profiles of various pyrolysis products in the gas-phase (H, NH, C₂) in Fig. 12(b). On the basis of this

¹ A detailed analysis of the char layer density is presented in the next section.

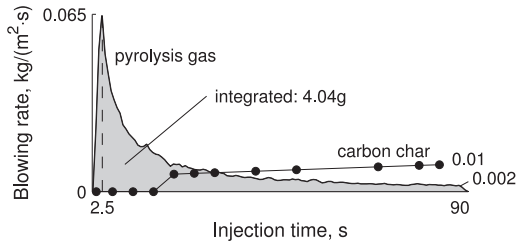


Fig. 13. Temporal pyrolysis blowing rate processed for Asterm ablation (AS-A3a) based on measured hydrogen (H_2) emission and mass loss due to pyrolysis outgassing \dot{m}_{pg} (Table 3); the momentaneous char blowing rate is given as well (AS-A3a, 1 MW/m², 200 hPa).

evidence, it seems fair to suggest that the increasing temperature in the boundary layer for a given spectrometer does not have significant impact on the temporal pyrolysis profile. In other words, it is not important at which distance from the surface the normalized temporal profile of H_2 -emission is taken.

The resulting temporal pyrolysis outgassing peaked shortly after sample injection at 0.065 kg/(m² s) (Fig. 13), but decreased rapidly during the first seconds. In addition, the temporal carbon blowing rate, based on the recession rate (Fig. 10) and a char density of 225 kg/m³, is shown.¹ A second order polynomial fit to the recession data provided the instantaneous recession rate for each time step. This enabled evaluation of ablation rates for the corresponding pyrolysis blowing rates at the same instant of time. These data will be presented together with the numerical results for better comparison in Section 4.2.

4.2. Numerical approach

Following the approach of Kendall et al. [20], thermochemical tables (B' -tables) are widely used to estimate the char consumption of an ablating surface as a function of the pyrolysis gas mass flow, the temperature, and pressure. Surface mass and energy balances at thermodynamic equilibrium couples the atmosphere of interest with the surface char and the pyrolysis products. A schematic of the surface mass and energy balances of a generic ablating, or “active” surface is presented in Fig. 14, with an imaginary thin control volume fixed to the receding wall. Heat and mass transfer-coefficients correlate the convective heat and mass transfer rates at the ablating surface to the flow environment at the edge of the boundary layer, without the need to fully couple the flow environment [47]. The thermochemical tables obtained from this approach, specific for one TPM composition and atmosphere, relate surface temperature and pressure to a dimensionless surface mass flux.

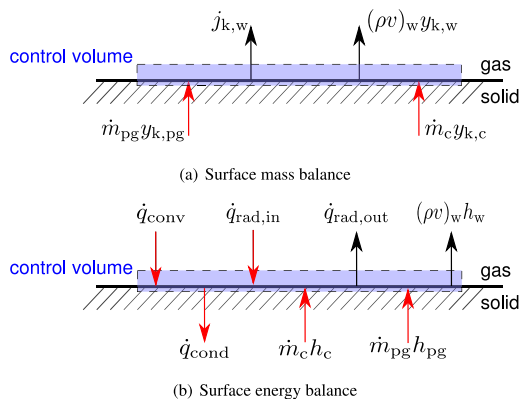


Fig. 14. Overall mass fluxes including compositions (a) and energy fluxes (b) in a control volume fixed to the surface of a generic ablative material.

Neglecting species condensation at the surface, the mass conservation equation of element k (e.g. C, H, N, O) for the control volume can be written as follows

$$\dot{m}_{pg} y_{k,pg} + \dot{m}_c y_{k,c} = (\rho v)_w y_{k,w} + j_{k,w}, \quad (6)$$

with the left-hand side terms being the mass ejected by the material: $y_{k,pg}$ and $y_{k,c}$ are the mass fraction of each element k in the pyrolysis gas ($=0$ if non-pyrolyzing), and the char, respectively. Quantities \dot{m}_{pg} and \dot{m}_c are the pyrolysis gas mass flux and the char mass consumption rate (kg/(m² s)). The fluxes away from the surface are the diffusive flux j_k and the motion of the fluid at velocity v due to the inserted mass (\dot{m}), with $y_{k,w}$ as the mass fraction of each element at the wall. Since mass is only inserted by the surface heterogeneous reactions, summing up Eq. (6) over all elements k ($\sum_k j_{k,w} = 0$ due to mass conservation) yields the global surface mass balance,

$$\dot{m}_{pg} + \dot{m}_c = (\rho v)_w, \quad (7)$$

with $\dot{m}_{pg} + \dot{m}_c$ being the total material mass loss rates.

Analogous to the mass conservation discussed above, incoming energy fluxes to the control volume are the convective heat flux (\dot{q}_{conv}) including diffusion, possible radiation from the boundary layer ($\dot{q}_{rad,in}$), and the enthalpy fluxes due to the solid material consumption ($\dot{m}_c h_c + \dot{m}_{pg} h_{pg}$). Energy fluxes leaving the control volume include surface radiation ($\dot{q}_{rad,out}$), material conduction (\dot{q}_{cond}), and the enthalpy flux carried by the species “blown” from the surface ($(\rho v)_w h_w$). The global energy conservation is thus given by

$$\dot{q}_{conv} + \dot{q}_{rad,in} + \dot{m}_c h_c + \dot{m}_{pg} h_{pg} = (\rho v)_w h_w + \dot{q}_{rad,out} + \dot{q}_{cond}, \quad (8)$$

with surface entering fluxes on the left-hand side and exiting energy fluxes on the right-hand side. At low enough freestream gas temperatures, the incoming gas radiation $\dot{q}_{rad,in}$ can be neglected and the outgoing radiation emitted by the surface reads

$$\dot{q}_{rad,out} = \varepsilon \sigma T_w^4. \quad (9)$$

In our case, the surface energy balance is obsolete as the measured surface temperature will be directly used for the computation. However, the approach is shown for completeness.

The diffusion flux $j_{k,w}$ of the elements in the mixture can be computed using the transfer potential method that assumes equal mass diffusion coefficients for all species in the mixture

$$j_{k,w} = C_M (y_{k,w} - y_{k,e}), \quad (10)$$

with C_M being the dimensional mass transfer coefficient [kg/(m² s)]. Substituting Eq. (10) and (7) into (6) provides the char consumption rate in dependence of the pyrolysis mass flux,

$$\dot{m}_c = \frac{\dot{m}_{pg} (y_{k,w} - y_{k,pg}) + C_M (y_{k,w} - y_{k,e})}{y_{k,c} - y_{k,w}}. \quad (11)$$

Division by C_M yields the non-dimensional mass blowing parameters $B'_g = \dot{m}_{pg}/C_M$ and $B'_c = \dot{m}_c/C_M$. The composition at the wall ($y_{k,w}$) can then be computed based on thermochemical equilibrium for a given B'_g and starting from an initial guess of B'_c by

$$y_{k,w} = \frac{B'_g y_{k,pg} + B'_c y_{k,c} + y_{k,e}}{B'_g + B'_c + 1}. \quad (12)$$

The elemental compositions of the pyrolysis gas ($y_{k,pg}$), char ($y_{k,c}$), and boundary layer edge ($y_{k,e}$) are given as we will describe shortly. The mass-transfer coefficient C_M is still required for a full description of the problem. In a fluid flow with heat and mass transfer, thermal diffusivity α and mass diffusivity \mathcal{D} are related by the Lewis number

$$Le = \frac{\alpha}{\mathcal{D}}. \quad (13)$$

Assuming equal mass and energy transfer coefficients, i.e., $Le = 1$, and applying a blowing correction for the mass injection at the surface [48,49], we obtain

$$C_M = C_H = C_{H_0} \frac{\ln(1 + 2KB')}{2KB'} \quad (14)$$

with C_H being a corrected heat transfer coefficient, $B' = B'_c + B'_g$, and K a factor depending on the flow regime (we assume $K = 0.5$ for laminar flow). Assuming that the viscous dissipation in the boundary layer equals heat conduction, the Prandtl number equals one,

$$Pr = \frac{\mu C_p}{k} = \frac{\nu}{\alpha} \quad (15)$$

and the boundary layer heat transfer coefficient C_{H_0} can be approximated from the measured cold wall heat flux \dot{q}_{cw} and the computed boundary layer edge enthalpy h_e and cold-wall enthalpy h_{cw} ,

$$C_{H_0} = \frac{\dot{q}_{cw}}{(h_e + \frac{1}{2}v_e^2 - h_{cw})} \quad (16)$$

In this case equal heat and mass transfer coefficients are assumed, independent of the wall condition (hot ablating wall, or cold wall calorimeter measurement). The non-equilibrium boundary layer computation provided the cold-wall enthalpy h_{cw} , instead of an equilibrium enthalpy at 350 K (temperature of the calorimeter). It is based on the calorimeter recombination efficiency γ . C_{H_0} was provided for each test condition through Eq. (16) by the numerical rebuilding procedure (Table 1). C_M was then available as function of the boundary layer edge condition without ablation.

For comparison with the experimental data and better understanding, the dimensionless blowing rates B'_c and B'_g can be converted to ablation rate by

$$\dot{s}_c = \frac{\dot{m}_c}{\rho_c} = \frac{B'_c C_M}{\rho_c} \quad (17)$$

and pyrolysis blowing rate ($\dot{m}_g = B'_g C_M$).

We used the thermochemical library MUTATION⁺⁺ [50–52] for computation of B'_c based on B'_g with an initial elemental composition for the resin (C_6H_5OH), mixed with air (21% O, 79% N). The initial elemental composition ($y_{k,pg}$) was calculated based on pure resin (Table 4), and assuming that a certain percentage of the mixture, by mass, will be transformed into solid char of pure carbon, staying within the material. This char yield fraction (Y_{char}) was removed from the pyrolysis gas mixture, with the rest of the pyrolysis gases mixing with the air. The new pyrolysis gas composition was computed based on the new molar content of carbon X_C , which was obtained from pure phenol as initial composition,

$$X_C = \frac{\mathcal{M}_{C_6H_5OH}(1 - Y_{char}) - \mathcal{M}_O - 6\mathcal{M}_H}{\mathcal{M}_C} \quad (18)$$

with \mathcal{M} being the molecular mass of the respective constituents.

A scheme illustrating the procedure for computation of ablation rates is given in Fig. 15. Numerical simulation of the plasma flow field and the boundary layer code provided the required condition at the boundary layer edge (Table 1). Knowledge of the boundary layer edge enthalpy (h_e) and the cold-wall heat flux allowed com-

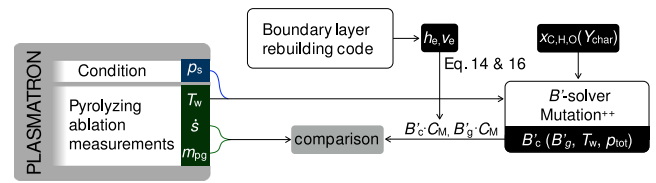


Fig. 15. Ablation computation procedure: Experimentally measured surface temperature and pressure as well as pyrolysis gas composition based on char yield (Y_{char}) are input for computation of thermochemical ablation (B' -tables) using MUTATION⁺⁺; the numerical simulation of the boundary layer edge condition (enthalpy h_e) serves for computation of the ablation and pyrolysis blowing rates.

putation of the dimensional ablation and pyrolysis blowing rates based on C_M following Eq. 14 and 16.

A char yield close to 50% is a common assumption for PICA-like materials [53], but should ideally be determined, for instance, by Thermal Gravimetric Analysis (TGA). We estimated the virgin Asterm density to be 265 kg/m³, and it is made up of approximately 30% phenolic resin. Hence, a 50% char yield would result in a char density of $\rho_c = 225.3$ kg/m³. MUTATION⁺⁺ assumes the char composition at the wall to be solid graphite. We computed the ablation rates for three different pyrolysis gas elemental compositions, resulting from char yields of 40%, 50%, and 65%. The elemental composition of the pyrolysis gas as a result of each char yield is listed in Table 4.

The computed ablation rates are presented together with the experimental measurements in Fig. 16 for all four test conditions according to low pressure conditions AS-A1a (Fig. 16(a)), and AS-A1b (Fig. 16(c)), as well as high pressure conditions AS-A3a (Fig. 16(b)), and AS-A3b (Fig. 16(d)). Each of the lines represents the computed carbon consumption rate for a wide range of pyrolysis gas blowing rates. Bullets represent the experimental data including error bars.

Regarding the experimental data, no recession was observed for all conditions right after injection of the sample, i.e., at high pyrolysis blowing rates. Although no temporal axis is shown, the test time can be imagined to increase from right to left as indicated in Fig. 16(a), i.e., at decreasing pyrolysis blowing rates (consistent with Fig. 13). At high pressure tests (200 hPa (b) and (d)), the ablation rate increased with decreasing pyrolysis blowing. This was less pronounced at lower pressure (15 hPa (a) and (b)), where especially the high heating condition (AS-A1b at 3 MW/m²) responded with an almost steady ablation rate.

The measured surface temperature T_w and the experimental pressure p_s of each test condition served as input for the $B'_c(T_w, p, B'_g)$ computation. Fig. 16 serves to illustrate the general trend of surface ablation vs. pyrolysis gas blowing rate: The surface ablation rate equals zero for char yields of 50% or lower at high pyrolysis gas blowing rates ($B'_c = 0$), as all oxygen is consumed by the carbon ejected by the pyrolysis gas into the boundary layer. At decreasing pyrolysis gas blowing, the ablation rate increases with a maximum at $B'_g = 0$, where all oxygen diffusing through the boundary layer is consumed at the surface. Note that these curves are computed based on thermochemical equilibrium.

In general, the B' -table approach underpredicted experimental ablation rates. This is especially apparent for low pressure tests (39% for AS-A1a, Fig. 16(a) and 24% for AS-A1b, 16(c)). The numerical ablation rates closely matched the experiment at high pressure but low heat flux (Fig. 16(b)). At high heating conditions, the experimental data could be matched with a char yield of 65% at high pyrolysis blowing rates (AS-A1b and AS-A3b, Fig. 16(c) and (d)). However, for pure char ablation without pyrolysis outgassing, recession is still underpredicted by within 20%. Varying pyrolysis gas compositions based on char yields between 40% and 65% strongly influenced the computed ablation rates within the

Table 4

Pyrolysis gas elemental compositions by mole for different char yields (by mass) for computation of thermochemical equilibrium tables.

Char yield	Carbon	Hydrogen	Oxygen
0	0.4615	0.4615	0.0769
40	0.291	0.608	0.101
50	0.229	0.661	0.110
65	0.115	0.759	0.126

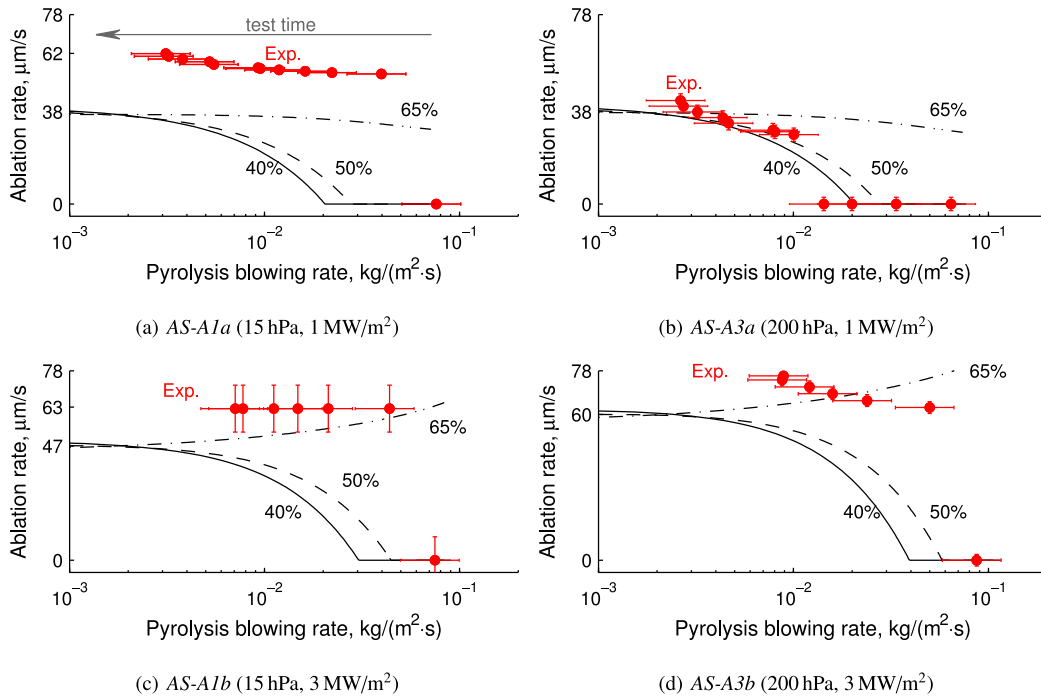


Fig. 16. Experimental ablation rates (symbols) compared with simulated carbon ablation rates (lines) for four Astern test conditions computed at the measured surface temperature T_w ; The simulated curves are based on a B' -table approach ($\dot{m}_c = B'_c C_M$) and were computed for a range of pyrolysis gas blowing rates (B'_g), and different pyrolysis gas compositions according to char yields of 40%, 50%, and 65%. The pyrolysis gas composition (Table 4) influences the ablation rate especially at high pyrolysis blowing rates.

observed range of experimental pyrolysis blowing rates. This can be assigned to the reduced carbon available in the pyrolysis gas at higher char yields, especially at pyrolysis blowing rates exceeding $0.005 \text{ kg}/(\text{m}^2 \text{ s})$. With high pyrolysis gas blowing rates at high char yields additional oxygen coming from the phenolic resin is injected into the boundary layer leading to higher surface ablation rates. The different char densities, based on the phenolic char yield (Eq. 17), marginally influenced the ablation rate when pyrolysis blowing was negligible ($\dot{m}_{pg} \rightarrow 0$).

4.3. Discussion of experimental and numerical approaches

The available evidence suggests a strong deviation of experimental ablation rates from predictions following the B' -tables approach, especially at low pressure (15 hPa). We will first discuss the numerical procedure in order to find possible reasons for this deviation, followed by a discussion regarding the experimental data.

4.3.1. Numerical approach.

A strong assumption has been made regarding the chemically reacting boundary layer, applying heat and mass transfer coefficients to the ablation computations. Those relate the wall condition to that at the boundary layer edge through species fraction differences across the boundary layer as the driving potential. Real diffusion in the gas-phase is not computed but might be higher in the experiments than represented by the mass transfer coefficient. In addition, the boundary layer, as well as the surface, may not be in thermochemical equilibrium at low pressure. We presented in another reference temperature measurements in the boundary layer from ablation originated CN violet emission that suggested a deviation from thermal equilibrium at pressures of 15 hPa [28]. But despite those indications of possible non-equilibrium at the wall, thermochemical equilibrium is usually an upper bound assumption that would lead to an overestimation of ablation rates rather than underestimation as in our case. In order to better address diffusion through the boundary layer we suggest a coupled

computation of material response and flow field, for example, by a simplified stagnation line description. This was already performed by Turchi et al. [47] for the non-pyrolyzing CBCF preform. Applying finite-rate chemistry at the reacting wall would help to further research the gas/surface interaction. Additionally, we suggest a sensitivity analysis of the boundary layer rebuilding procedure as both the edge enthalpy h_e and the cold-wall enthalpy h_w are based on the cold-wall calorimeter recombination efficiency γ . An inaccurate assumption for γ affects the heat transfer coefficient C_H . Both investigations are currently ongoing.

Further, the char layer, composed of the carbonized resin and the remaining carbon fibers, is treated as homogeneous solid carbon. But the reactivity of the carbonized matrix was suggested to be approximately 10 times higher than that of the fibers for those types of materials [22]. Our micrographs support this assertion, as no charred resin was found directly at the surface where the fibers were oxidized. Hence, treating the carbonized resin and carbon fibers separately in the numerical model may help to increase the recession rates towards the experimental observations.

4.3.2. Experimental approach

Instead of underpredicted recession rates, the ablation experiment might be falsified, leading to too high material recession compared with pure thermochemical equilibrium ablation. Mechanical erosion of the charred surface was first ruled out as cause for an overshoot of experimental ablation rates for our test conditions. Shear stresses in the subsonic flow field are very low due to the low flow velocity and gas density. The corresponding test in nitrogen showed almost no ablation of the surface although flow velocities (and dynamic pressures) at 15 hPa were very similar to those in air, in the order of 220 m/s (AS-A1a, AS-N1a) and 530 m/s to 670 m/s (AS-A1b, AS-N1b), respectively (Table 1). However, research during the last years provided ample support for the assertion that the porous micro-structure of the materials considered in this study may develop an ablation zone in the subsurface char layer [22,23,54]. Their work propounds the view that at a high

diffusion rate of oxygen compared with the oxidation reaction rate, the oxidant concentration can become homogeneous inside the porous char and ablation occurs in volume. In that case, ablation of the char layer and carbon fibers from within could lead to higher ablation rates due to a weakened fiber structure. Convection of oxygen into the porous material due to a higher stagnation point pressure compared to the sidewall static pressure offers a similar explanation. This would weaken the char-fiber structure by oxidation from within, leading to detachment of fiber fragments once the surrounding fibers ablate. This scenario would be a combination of chemical and mechanical ablation. A 3D numerical study of low-density carbon-phenolic samples has shown the strong influence of side-wall outgassing on the porous material [18]. In this case, the pyrolysis gases created inside the material may leave from the sidewall instead of blocking the boundary layer gases at the stagnation point. However, Lachaud et al. showed in recent simulations that boundary layer gases penetrate the test sample only during the first fractions of a second. After that, the pyrolysis gases build up enough pressure against the oxygen from the boundary layer [19]. Simulations using a material response code should be performed in the future to confirm this for our experimental setup. However, this does not impact ablation rates at low pyrolysis gas blowing, as observed towards test end, for which the numerical model still underpredicts ablation rates. Lastly, recession rates of Astern and AQ61 were very similar, and both increasing with chamber pressure for a heat flux of 3 MW/m² (15 hPa and 200 hPa), from 47 μm/s to 83 μm/s for AQ61 (AQ-A1b → AQ-A3b) and from 62 μm/s to 71 μm/s for Astern (AS-A1b → AS-A3b), respectively. Although dynamic pressure was one order of magnitude lower at high chamber static pressure, the recession rate increased. Moreover, if mechanical erosion by in-depth oxidation occurred at low pressure, it should also be apparent for high heat flux tests (A1a → A1b). These resulted in even higher dynamic pressure and higher diffusion. But recession rates at low pressure were almost identical for the two heat fluxes at 15 hPa arguing against mechanical erosion at low chamber pressures. The micrographs of ablated samples support this argument. No oxidation of the charred material was observed below a depth of approximately 100 μm. Some spallation of samples was observed at high pressure conditions (200 hPa), but almost not visible at low pressure. We suggest additional studies for a detailed characterization of spallation phenomena during the experiments, for example by high-speed video imaging as performed by Martin et al. [55].

The highest experimental uncertainties were introduced by the surface area that was used for the computation of the pyrolysis blowing rate. We considered a constant outgassing rate over the hemisphere, justified by the sudden surface temperature rise during sample injection, setting the surface at a high enough temperature to cause pyrolysis. The maximum and minimum blowing rates were then obtained by considering or neglecting pyrolysis through the cylindrical sidewalls. However, this uncertainty has no influence on the measured recession rates, still putting the predicted recession rates at low pyrolysis blowing (towards test end) into question. Improvement of the experimental values is suggested, e.g., by scaling the pyrolyzing surface according to surface temperature mappings obtained using infrared-camera images. A camera with higher resolution would further improve the volumetric recession of the sample, possibly extended by additional cameras for 3D images as performed by Löhle et al. [56] during ablation tests. Further studies are also advised regarding the effects of sidewall pyrolysis outgassing. This may be either done during the experiment using impermeable sample holders or by a numerical analysis using 2D material response codes.

5. Conclusion

We performed ablation experiments of low density carbon-phenolic ablators in air and nitrogen plasmas to investigate ablation of the surface and the transient pyrolysis gases created by the material. Cold wall heat fluxes were 1 MW/m² and 3 MW/m² at test chamber pressures between 15 hPa and 200 hPa, resulting in surface temperatures of 1900 K to 2800 K and maximum surface recession rates in air plasma of 83 μm/s (5.0 mm/min).

Air ablation led to icicle shaping of fibers at the surface and charred resin was found ~50 μm below the surface. No internal oxidation was observed, arguing against an inflow of boundary layer gases into the porous material. Fully coupled material codes, able to represent the material's microstructure, are required to simulate the oxidation zone of the charred resin and carbon fibers at the surface. On the contrary to air, carbon deposition in the form of soot was confirmed on samples tested in nitrogen in the stagnation point region as well as at the side- and back-walls.

Emission spectra recorded in the boundary layer were indicative of reactive products that originated from pyrolysis outgassing (C₂, CH, CN, NH and OH). The time-resolved emission of species associated to the pyrolysis gases helped to rebuild the temporal pyrolysis outgassing profile. We proposed an approach to estimate the temporal pyrolysis outgassing rate, based on pre/post-ablation volume and mass measurements. The temporal recession rate was obtained from high-speed camera imaging. This enabled evaluation of the surface recession as a function of the pyrolysis outgassing rate, which was then compared to numerical estimates predicted by an approach using thermochemical tables at equilibrium (*B'*-tables).

In all cases, the thermochemical equilibrium model underpredicted the experimental recession rates, especially at low chamber pressure (15 hPa). Experimental recession rates at low chamber pressure did not increase with tripled heat flux, indicating diffusion-limited ablation. We showed that changes of the pyrolysis gas composition, caused by different char yields of the resin, strongly influence the surface ablation rate. However, this did not help to match all of the experimental data, especially at low heating and low pressure (1 MW/m², 15 hPa) the discrepancy between experiment and simulation persists. Stronger mechanical failure of the material due to high flow velocities at lower pressures may serve as explanation, although experiments at the same pressure and heat-flux conditions but in nitrogen plasma did not show any significant recession. If, however, oxygen is able to flow through the permeable char layer due to a higher stagnation point pressure compared to the sidewall static pressure, the interior char-fiber structure may be weakened by oxidation, followed by removal due to aerodynamic shear. This scenario would be a combination of chemical and mechanical ablation. However, no internal oxidation of the porous material was observed by scanning electron microscopy. Additionally, such chemical-mechanical ablation should also be apparent for high heat flux tests, which result in even higher dynamic pressure, and higher diffusion at higher wall temperatures. But this was not observed in the current ablation test campaign. No spallation was observed during the low pressure experimental runs.

In the case that mechanical erosion can be ruled out, the application of *B'*-tables for the ablation thermochemistry, including heat and mass transfer coefficients for the boundary layer, may not be sufficient for all test conditions. Both explanations, chemical-mechanical erosion and limited validity of the thermochemical table approach, require detailed numerical simulations of the microscale char layer for improved description of this problem. We further suggest investigation of the effects of sidewall pyrolysis outgassing.

Acknowledgements

We gratefully acknowledge Airbus DS for providing the test material, in particular Jean-Marc Bouilly and Gregory Pinaud for scientific discussions. The research of B. H. is supported by a fellowship of the Agency for Innovation by Science and Technology (IWT, dossier #111529) in Flanders, and research of J.B. S. and T. M. by the European Research Council Starting Grant #259354. P. Collin is acknowledged for his valuable help as Plasmatron operator.

References

- [1] G.W. Sutton, The initial development of ablation heat protection: an historical perspective, *J. Spacecraft Rock.* 19 (1) (1982) 3–11, <http://dx.doi.org/10.2514/3.62196>.
- [2] L. Torre, J. Kenny, A. Maffezzoli, Degradation behaviour of a composite material for thermal protection systems Part I – experimental characterization, *J. Mater. Sci.* 33 (1998) 3137–3143, <http://dx.doi.org/10.1023/A:1004399923891>.
- [3] G. Duffa, *Ablative Thermal Protection Systems Modeling*, AIAA Education Series, 2013.
- [4] H.K. Tran, Development of lightweight ceramic ablators and arc jet test results, NASA Ames Research Center, 1994. Technical Memorandum TM-108798.
- [5] H.K.K. Tran, C.E. Johnson, D.J. Rasky, F.C.L. Hui, M.T. Hsu, T. Chen, Y.K. Chen, D. Paragas, L. Kobayashi, Phenolic impregnated carbon ablators (PICA) as thermal protection systems for discovery missions, NASA Ames Research Center, 1997. Technical Memorandum TM 110440.
- [6] H. Ritter, P. Portela, K. Keller, J.-M. Bouilly, S. Burnage, Development of a European ablative material for heatshields of sample return missions, in: *6th European Workshop on TPS and Hot Structures*, Stuttgart, Germany, 2009.
- [7] M. Stackpoole, S. Sepka, I. Cozmuta, Post-flight evaluation of stardust sample return capsule forebody heatshield material, AIAA paper 2008-1202 Reno, NV, USA, 2008, doi: <http://dx.doi.org/10.2514/MASM08>.
- [8] K.T. Edquist, B.R. Hollis, C.O. Johnston, D. Bose, T.R. White, M. Mahzari, Mars science laboratory heatshield aerothermodynamics: design and reconstruction, 44th AIAA Thermophysics Conference, AIAA paper 2013-2781, San Diego, CA, USA, 2013, doi: <http://dx.doi.org/10.2514/MTP13>.
- [9] R.A.S. Beck, D.M. Driver, M.J. Wright, H.H. Hwang, K.T. Edquist, S.A. Sepka, Development of the mars science laboratory heat shield thermal protection system, *J. Spacecraft Rock.* 51 (2014) 1139–1150, <http://dx.doi.org/10.2514/1.A32635>.
- [10] B. Laub, E. Venkatapathy, Thermal protection system technology and facility needs for demanding future planetary missions, in: A. Wilson (Ed.), *International Workshop on Planetary Probe Atmospheric Entry and Descent Trajectory Analysis and Science*, ESA SP-544, Lisbon, Portugal, 2003, pp. 239–247.
- [11] R.K. Crouch, G.D. Walberg, An investigation of ablation behavior of avcoat 5026/39M over a wide range of thermal environments, NASA, 1969. Technical Memorandum TM X-1778.
- [12] G. Herdrich, M. Fertig, S. Löhle, Experimental simulation of high enthalpy planetary entries, *Open Plasma Phys. J.* 2 (2009) 150–164, <http://dx.doi.org/10.2174/1876534300902010150>.
- [13] D. M. Smith, T. Younker, Comparative ablation testing of carbon phenolic TPS materials in the AEDC-H1 arcjet, in: *AIAA/CIRA 13th International Space Planes and Hypersonics Systems and Technologies Conference*, AIAA paper 2005-3263, Capua, Italy, 2005, doi: <http://dx.doi.org/10.2514/MISPHST05>.
- [14] M.A. Covington, J.M. Heinemann, H.E. Goldstein, Y.K. Chen, I. Terrazas-Salinas, J.A. Balboni, J. Olejniczak, E.R. Martinez, Performance of a low density ablative heat shield material, *J. Spacecraft Rock.* 45 (4) (2008) 854–864, <http://dx.doi.org/10.2514/1.38249>.
- [15] D. Prabhu, D. Saunders, T. Oishi, K. Skokova, J. Santos, J. Fu, I. Terrazas-Salinas, E. Carballo, D. Driver, CFD analysis framework for arc-heated flowfields, I: stagnation testing in arc-jets at NASA ARC, in: *41st AIAA Thermophysics Conference*, AIAA paper 2009-4080, San Antonio, TX, USA, 2009, doi: <http://dx.doi.org/10.2514/MTC09>.
- [16] D.M. Driver, M. MacLean, Improved predictions of PICA recession in arc jet shear tests, in: *49th AIAA Aerospace Sciences Meeting including the New Horizons Forum and Aerospace Exposition*, AIAA paper 2011-141, Orlando, FL, USA, 2011, doi: <http://dx.doi.org/10.2514/MASM11>.
- [17] F. Milos, Y.-K. Chen, Ablation and thermal response property model validation for phenolic impregnated carbon ablator, *J. Spacecraft Rock.* 47 (5) (2010) 786–805, <http://dx.doi.org/10.2514/1.42949>.
- [18] H. Weng, S.C.C. Bailey, A. Martin, Numerical study of iso-Q sample geometric effects on charring ablative materials, *Int. J. Heat. Mass. Transf.* 80 (2015) 570–596, <http://dx.doi.org/10.1016/j.ijheatmasstransfer.2014.09.040>.
- [19] J. Lachaud, T. van Eekelen, J.B. Scoggins, T.E. Magin, N.N. Mansour, Detailed chemical equilibrium model for porous ablative materials, *Int. J. Heat. Mass. Transf.* 90 (2015) 1034–1045, <http://dx.doi.org/10.1016/j.ijheatmasstransfer.2015.05.106>.
- [20] R.M. Kendall, E.P. Bartlett, R.A. Rindal, C.B. Moyer, An analysis of the coupled chemically reacting boundary layer and charring ablator: Part I, NASA, 1968. Tech. Rep. CR 1060.
- [21] F.S. Milos, Y.-K. Chen, Comprehensive model for multicomponent ablation thermochemistry, in: *35th Aerospace Sciences Meeting & Exhibit*, AIAA paper 1997-0141, Reno, NV, USA, 1997, doi: <http://dx.doi.org/10.2514/MASM97>.
- [22] J. Lachaud, I. Cozmuta, N. Mansour, Multiscale approach to ablation modeling of phenolic impregnated carbon ablators, *J. Spacecraft Rock.* 47 (6) (2010) 910–921, <http://dx.doi.org/10.2514/1.42681>.
- [23] J. Lachaud, N. Mansour, Microscopic scale simulation of the ablation of fibrous materials, in: *48th AIAA Aerospace Sciences Meeting Including the New Horizons Forum and Aerospace Exposition*, AIAA paper 2010-984, Orlando, FL, USA, 2010, doi: <http://dx.doi.org/10.2514/MASM10>.
- [24] J. Lachaud, N.N. Mansour, Porous-material analysis toolbox based on OpenFOAM and applications, *J. Thermophys. Heat Transfer* 28 (2) (2014) 191–202, <http://dx.doi.org/10.2514/1.T4262>.
- [25] H.-W. Wong, J. Peck, R. Edwards, G. Reinisch, J. Lachaud, N.N. Mansour, Measurement of pyrolysis products from phenolic polymer thermal decomposition, in: *52nd Aerospace Sciences Meeting*, AIAA paper 2014-1388, National Harbor, MD, USA, 2014, doi: <http://dx.doi.org/10.2514/masm14>.
- [26] B. Bottin, *Aerothermodynamic model of an inductively-coupled plasma wind tunnel Ph.D. thesis*, Université de Liège, von Karman Institute for Fluid Dynamics, 1999.
- [27] B. Bottin, O. Chazot, M. Carbonaro, V. van der Haegen, S. Paris, The VKI plasmatron characteristics and performance, in: *RTO AVT course on measurement techniques for high enthalpy and plasma flows*, RTO EN-8, Rhode-Saint-Genèse, Belgium, 1999, pp. 6-01–6-26.
- [28] B. Helber, O. Chazot, A. Hubin, T. Magin, Microstructure and gas-surface interaction studies of a low-density carbon-bonded carbon fiber composite in atmospheric entry plasmas, *Compos.: Part A* 72 (2015) 96–107, <http://dx.doi.org/10.1016/j.compositesa.2015.02.004>.
- [29] B. Helber, A. Turchi, O. Chazot, A. Hubin, T. Magin, Gas/surface interaction study of low-density ablators in sub35th aero and supersonic plasmas, in: *11th AIAA/ASME Joint Thermophysics and Heat Transfer Conference*, AIAA paper 2014-2122, Atlanta, GA, USA, 2014, doi: <http://dx.doi.org/10.2514/MTPHT14>.
- [30] Mersen (Brochure), *CALCARB rigid carbon thermal insulation*, 2015. URL <<http://www.mersen.com/uploads/txmersen/3-CALCARB-rigid-carbon-thermal-insulation-mersen12.pdf>>.
- [31] B. Helber, C.O. Asma, Y. Babou, A. Hubin, O. Chazot, T.E. Magin, Material response characterization of a low-density carbon composite ablator in high-enthalpy plasma flows, *J. Mater. Sci.* 49 (13) (2014) 4530–4543, <http://dx.doi.org/10.1007/s10853-014-8153-z>.
- [32] G. Degrez, D.P. Vanden Abeele, P.F. Barbante, B. Bottin, Numerical simulation of inductively coupled plasma flows under chemical non-equilibrium, *Int. J. Numer. Methods Heat Fluid Flow* 14 (4) (2004) 538–558, <http://dx.doi.org/10.1108/09615530410532286>.
- [33] D. Vanden Abeele, G. Degrez, Efficient computational model for inductive plasmas flows, *AIAA J.* 38 (2) (2000) 234–242, <http://dx.doi.org/10.2514/2.977>.
- [34] T.E. Magin, G. Degrez, Transport algorithms for partially ionized and unmagnetized plasmas, *J. Comput. Phys.* 198 (2004) 424–449, <http://dx.doi.org/10.1016/j.jcp.2004.01.012>.
- [35] P. Barbante, G. Degrez, G. Sarma, Computation of nonequilibrium high temperature axisymmetric boundary-layer flows, *J. Thermophys. Heat Transfer* 16 (4) (2002) 490–497, <http://dx.doi.org/10.2514/2.6723>.
- [36] S. Farhan, L. Ke-zhi, G. Ling-jun, G. Quan-ming, L. Feng-tao, Effect of density and fibre orientation on the ablation behavior of carbon-carbon composites, *New Carbon Mater.* 25 (3) (2010) 161–166, [http://dx.doi.org/10.1016/S1872-5805\(09\)60023-8](http://dx.doi.org/10.1016/S1872-5805(09)60023-8).
- [37] D. Cho, B. Yoon, I. Microstructural interpretation of the effect of various matrices on the ablation properties of carbon-fiber-reinforced composites, *Compos. Sci. Technol.* 61 (2001) 271–280, [http://dx.doi.org/10.1016/S0266-3538\(00\)00212-8](http://dx.doi.org/10.1016/S0266-3538(00)00212-8).
- [38] G. Duffa, G.L. Vignoles, J.-M. Goughéneche, Y. Aspa, Ablation of carbon-based materials: investigation of roughness set-up from heterogeneous reactions, *Int. J. Heat. Mass. Transf.* 48 (16) (2005) 3387–3401, <http://dx.doi.org/10.1016/j.ijheatmasstransfer.2005.02.036>.
- [39] J. Lachaud, Y. Aspa, G. Vignoles, Analytical modeling of the steady state ablation of a 3D C/C composite, *Int. J. Heat Mass Transf.* 51 (2008) 2614–2627, <http://dx.doi.org/10.1016/j.ijheatmasstransfer.2008.01.008>.
- [40] H. Wang, Formation of nascent soot and other condensed-phase materials in flames, *P. Combust. Inst.* 33 (1) (2011) 41–67, <http://dx.doi.org/10.1016/j.proci.2010.09.009>.
- [41] M.E. MacDonald, C.M. Jacobs, C.O. Laux, F. Zander, R. Morgan, Measurements of air plasma/ablator interactions in a 50 kw inductively coupled plasma torch, *J. Thermophys. Heat Transfer* 46 (3) (2015) 481–491, <http://dx.doi.org/10.2514/1.T4402>.
- [42] K.A. Trick, T.E. Saliba, Mechanisms of the pyrolysis of phenolic resin in a carbon/phenolic composite, *Carbon* 33 (11) (1995) 1509–1515, [http://dx.doi.org/10.1016/0008-6223\(95\)00092-R](http://dx.doi.org/10.1016/0008-6223(95)00092-R).
- [43] J. Uhl, W.P. Owens, J.M. Meyers, D.G. Fletcher, Pyrolysis simulation in an ICP torch facility, in: *42nd AIAA Thermophysics Conference*, AIAA paper 2011-3618, 2011.
- [44] R. Wernitz, C. Eichhorn, T. Marynowski, G. Herdrich, Plasma wind tunnel investigation of european ablators in nitrogen/methane using emission spectroscopy, *Int. J. Spectrosc.* 2013 (2013) 1–9, <http://dx.doi.org/10.1155/2013/764321>.

- [45] T. Kruse, P. Roth, Kinetics of C_2 reactions during high-temperature pyrolysis of acetylene, *J. Phys. Chem.* 101 (1997) 2138–2146, <http://dx.doi.org/10.1021/jp963373o>.
- [46] T. Hermann, S. Löhle, P. Leyland, L. Marraffa, J.-M. Bouilly, S. Fasoulas, First results on ablation radiation coupling through optical emission spectroscopy from the vacuum ultraviolet to the visible, in: 8th European Symposium on Aerothermodynamics for Space Vehicles, ESA ESTEC, Lisbon, Portugal, 2015.
- [47] A. Turchi, B. Helber, A. Munafò, T.E. Magin, Development and testing of an ablation model based on plasma wind tunnel experiments, in: 11th AIAA/ASME Joint Thermophysics and Heat Transfer Conference, AIAA paper 2014–2125, Atlanta, Georgia (USA), 2014. doi: <http://dx.doi.org/10.2514/MTPHT14>.
- [48] D.B. Spalding, *Convective Mass Transfer, An Introduction*, Edward Arnold, London, 1963.
- [49] W.M. Kays, M.E. Crawford, *Convective Heat and Mass Transfer*, McGraw-Hill, New York, 1980.
- [50] T. Magin, A model for inductive plasma wind tunnels Ph.D. thesis, Université libre de Bruxelles, von Karman Institute for Fluid Dynamics, 2004.
- [51] J.B. Scoggins, T. Magin, Development of MUTATION⁺⁺: MULTicomponent Thermodynamics And Transport properties for IONized gases library in C⁺⁺, in: 11th AIAA/ASME Joint Thermophysics and Heat Transfer Conference, AIAA paper 2014–2966, Atlanta, GA, USA, 2014. doi: <http://dx.doi.org/10.2514/MTPHT14>.
- [52] J.B. Scoggins, T.E. Magin, Gibbs function continuation for linearly constrained multiphase equilibria, *Combust. Flame* 162 (2015) 4514–4522, <http://dx.doi.org/10.1016/j.combustflame.2015.08.027>.
- [53] J. Rabinovitch, V.M. Marx, G. Blanquart, Pyrolysis gas composition for a phenolic impregnated carbon ablator heatshield, in: 11th AIAA/ASME Joint Thermophysics and Heat Transfer Conference, AIAA paper 2014–2246, Atlanta, GA, USA, 2014. doi: <http://dx.doi.org/10.2514/MTPHT14>.
- [54] F. Panerai, A. Martin, N.N. Mansour, S.A. Sepka, J. Lachaud, Flow-tube oxidation experiments on the carbon preform of a phenolic-impregnated carbon ablator, *J. Thermophys. Heat Transfer* 28 (2) (2014) 181–190, <http://dx.doi.org/10.2514/1.T4265>.
- [55] A. Martin, S.C.C. Bailey, F. Panerai, R.S.C. Davuluri, A.R. Vazsonyi, H. Zhang, Z.S. Lippay, N.N. Mansour, J.A. Inman, B.F. Bathel, S.C. Splinter, P.M. Danehy, Preliminary numerical and experimental analysis of the spallation phenomenon, in: 8th European Symposium on Aerothermodynamics for Space Vehicles, no. ESA ATD-88621, Lisbon, Portugal, 2015.
- [56] S. Löhle, T. Staebler, T. Reimer, A. Cefalu, Photogrammetric surface analysis of ablation processes in high enthalpy air plasma flow, in: 11th AIAA/ASME Joint Thermophysics and Heat Transfer Conference, AIAA paper 2014–2248, Atlanta, GA, USA, 2014. doi: <http://dx.doi.org/10.2514/MTPHT14>.